

An Introduction to the Application of Marine Controlled-Source Electromagnetic Methods for Natural Gas Hydrate Exploration

Li, Y.; Slob, E.C.; Werthmüller, D.; Wang, Lipeng ; Lu, Hailong

DOI

[10.3390/jmse11010034](https://doi.org/10.3390/jmse11010034)

Publication date

2023

Document Version

Final published version

Published in

Journal of Marine Science and Engineering

Citation (APA)

Li, Y., Slob, E. C., Werthmüller, D., Wang, L., & Lu, H. (2023). An Introduction to the Application of Marine Controlled-Source Electromagnetic Methods for Natural Gas Hydrate Exploration. *Journal of Marine Science and Engineering*, 11(1), Article 34. <https://doi.org/10.3390/jmse11010034>

Important note

To cite this publication, please use the final published version (if applicable). Please check the document version above.

Copyright

Other than for strictly personal use, it is not permitted to download, forward or distribute the text or part of it, without the consent of the author(s) and/or copyright holder(s), unless the work is under an open content license such as Creative Commons.

Takedown policy

Please contact us and provide details if you believe this document breaches copyrights. We will remove access to the work immediately and investigate your claim.

Article

An Introduction to the Application of Marine Controlled-Source Electromagnetic Methods for Natural Gas Hydrate Exploration

Yuan Li ^{1,2,3,*}, Evert Slob ² , Dieter Werthmüller ² , Lipeng Wang ⁴ and Hailong Lu ^{3,*}

¹ Department of Computer Science, Beijing Information Science and Technology University, Beijing 100192, China

² Department of Geoscience and Engineering, Delft University of Technology, Stevinweg 1, 2628CN Delft, The Netherlands

³ Beijing International Centre for Gas Hydrate, School of Geophysics and Information Technology, Peking University, Beijing 100871, China

⁴ Beihang University, Beijing 100191, China

* Correspondence: y.li-36@tudelft.nl (Y.L.); hlu@pku.edu.cn (H.L.); Tel.: +86-18801087009 (Y.L.)

Abstract: Natural gas hydrates have been an unconventional source of energy since the beginning of this century. Gas-hydrate-filled reservoirs show higher resistivity values compared with water-filled sediments. Their presence can be detected using marine controlled-source electromagnetic methods. We classify acquisition configurations into stationary and moving receiver configurations, which are described in terms of the design group, the operational details, and where they have been used successfully in the field for natural gas hydrate exploration. All configurations showed good numerical results for the detection of a 700 m long gas hydrate reservoir buried 200 m below the seafloor, but only the stationary configurations provided data that can be used to estimate the horizontal boundaries of the resistive part of the reservoir when the burial depth is known from seismic data. We discuss the operational steps of the configurations and provide the steps on how to choose a suitable configuration. Different CSEM configurations were used together with seismic data to estimate the edge of the gas hydrate reservoir and the total volume of the gas hydrates, to optimize the drilling location, to increase production safety, and to improve geological interpretations. It seems that CSEM has become a reliable method to aid in the decision-making process for gas hydrate reservoir appraisal and development.

Keywords: marine electromagnetic; natural gas hydrates; exploration; resistivity



Citation: Li, Y.; Slob, E.; Werthmüller, D.; Wang, L.; Lu, H. An Introduction to the Application of Marine Controlled-Source Electromagnetic Methods for Natural Gas Hydrate Exploration. *J. Mar. Sci. Eng.* **2023**, *11*, 34. <https://doi.org/10.3390/jmse11010034>

Academic Editor: Dejan Brkić

Received: 11 November 2022

Revised: 11 December 2022

Accepted: 15 December 2022

Published: 27 December 2022



Copyright: © 2022 by the authors. Licensee MDPI, Basel, Switzerland. This article is an open access article distributed under the terms and conditions of the Creative Commons Attribution (CC BY) license (<https://creativecommons.org/licenses/by/4.0/>).

1. Introduction

Natural gas hydrates, a potentially important energy resource, are abundant in seafloor sediments along the continental margins. Buried in the sediment below the seafloor, free gas may accumulate and form into solids under low-temperature and high-pressure conditions [1,2]. One cubic meter of in situ solid gas hydrates is equivalent to 164 cubic meters of free gas under atmospheric conditions [3–5]. Offshore gas hydrate reservoirs may become an important source of gas that could reduce the need for conventional fossil energy sources such as oil and coal and could possibly be economically produced in the future [6]. The exploitation of gas hydrates has challenges such as environmental pollution and increasing geohazards in the marine environment [7].

During gas hydrate accumulation, the phase may be a complicated and unpredictable mix of solid, gas, and liquid phases [8]. As the resistivity of methane hydrate is 50 kΩm according to laboratory experiment results [9], the presence of gas hydrates changes the geophysical properties of the layer. For example, a sediment layer containing gas hydrates shows different acoustic wave velocity and electric resistivity values than a sediment without gas hydrates. Therefore, geophysical methods such as seismic, electromagnetic, and gravity are used to map the sub-seafloor sediment structure to detect and localize

zones with anomalous properties [10,11]. A significant seismic signal called the bottom-simulating reflector (BSR) is used to identify the presence of gas hydrates [12,13]. It has been used to image the outer boundary of the gas hydrate stability field in sediment structures. According to the log data of many gas hydrate exploration findings, the presence of the BSR signal was not sufficient to verify the existence of gas hydrates [3]. Hence, the BSR does not always express a direct relationship with the presence of hydrates. While drilling provides direct evidence of its existence, we can also use the strong correlation of electric resistivity anomalies with the existence of gas hydrates to improve its exploration [14–17]. The layer containing gas hydrates shows anomalous values in resistivity, P-wave (V_p), and S-wave (V_s) curves in the drilling data of gas hydrate exploration [18].

Sediments containing a mix of brines and gas hydrates have reported bulk resistivity values of up to 100 times higher than sediments with only brines and appear more resistive than the surrounding rock. The resistivity may change from 3 Ωm to 200 Ωm between the sediments where gas hydrates are absent and present [3,4,19]. Taking these results into account, the marine controlled-source electromagnetic (CSEM) method could be a good choice to detect and characterize accumulations of gas hydrates. CSEM is sensitive to resistive material with a large lateral extent below the seafloor, like gas hydrates [20,21]. CSEM methods are useful to determine the prospect of structures imaged from seismic data before drilling, to map the distribution of hydrates in the seafloor sediments, and to estimate the volume of the gas hydrates.

For gas hydrates in sandy sediments, Archie's law can be used to estimate the total volume of hydrate in place [22]. Usually a modified version is used in which tortuosity is added to Archie's equation, which is given by:

$$\rho = a\rho_w S^{-n} \varphi^{-m}, \quad (1)$$

where a is called the tortuosity factor; m represents the cementation exponent; n represent the saturation exponent; ρ and ρ_w are bulk and water resistivity, respectively; φ is the porosity; and S is saturation. Some authors [23–26] have shown that a , n , and m should not be taken as constant but as a function of space depending on the field with an aim to provide a quantitative basis for gas hydrate volume estimation [4,27].

With the progress in numerical and physical experiments, CSEM has become a useful complementary method for gas hydrate detection. Various reviews of CSEM developments have been published [21,28–30]. Edwards listed the MCSEM according to the principles, methodologies, and commercial applications [21]. Constable provided an introduction to MCSEM and summarized the development of the CSEM method in the period of 2000 to 2010 for hydrocarbon exploration [28,30,31]. Key discussed marine EM methods for resource exploration and tectonic investigations [29]. In these reviews, acquisition geometries were not discussed, and no review has been published about the CSEM method that was dedicated to gas hydrate exploration. In addition, the relationship between the exploration target of gas hydrates and the acquisition geometry has not been considered. These are the topics of this paper.

Here, we first explain the differences between gas hydrate and traditional hydrocarbon reservoirs. In the next section, the electric field amplitudes are compared for situations in which gas hydrates are present or absent in the sediment. Then, the acquisition configurations that have been applied for gas hydrate exploration are described in terms of their advantages and disadvantages with considerations regarding how to choose the acquisition to start the survey. Finally, we discuss several typical applications of the configurations on the different characters of gas hydrates. We provide four goals of a MCSEM method for gas hydrate exploration and discuss how to choose an effective acquisition configuration.

2. How Is CSEM Being Used for Gas Hydrate Exploration?

CSEM is sensitive to resistive formations and has been applied successfully to study the upper oceanic lithosphere and to search for hydrocarbon reservoirs [31,32]. However, gas hydrate exploration cannot be simply copied from oil or gas exploration or lithospheric

studies. For example, gas hydrates are buried only up to a few hundred meters under the seafloor, not kilometers deep like oil marine reservoirs. In addition, conventional oil does not involve a phase transition, while gas hydrates have solid state to fluid phases.

First, we focus on the resistivity of the reservoirs. In Figure 1, we can see that sedimentary rocks express a wide range of resistivity values. This range is mostly determined by formation water content. For seawater-filled sediments, the bulk resistivity is usually around 1 Ω m. The resistivity of pure gas hydrates is up to four orders of magnitude higher according to experimental results [9]. Gas hydrates detected with geophysical methods have an electric resistivity that is up to two orders of magnitude higher. Compared with pure gas hydrates, a marine sediment filled with gas hydrates may have a lower resistivity, but it will still be higher than that of a seawater-filled sediment.

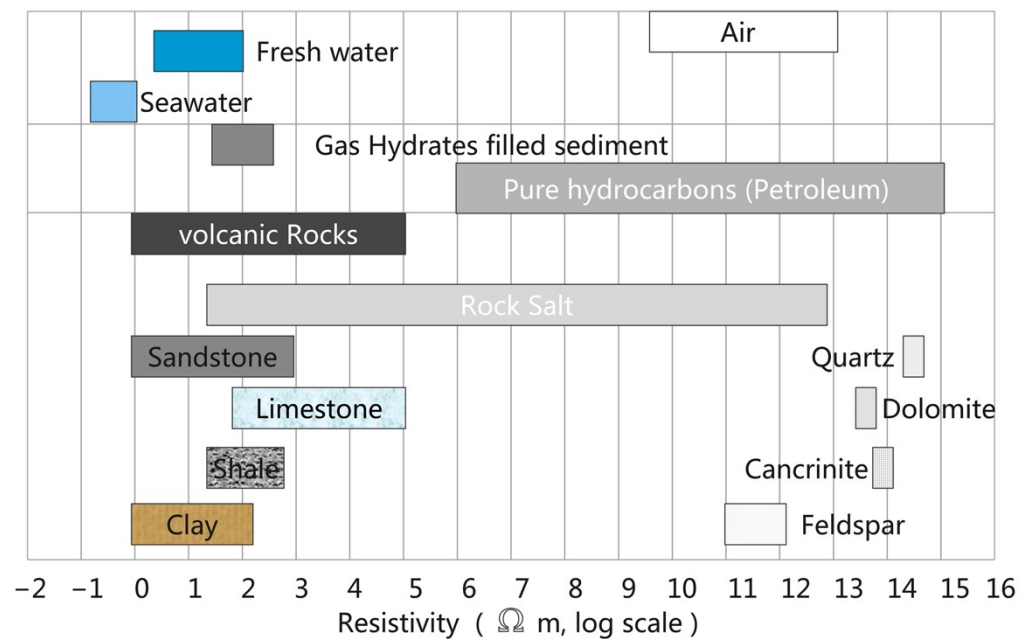


Figure 1. Resistivity ranges of different common materials. The resistivity of crystalline and volcanic rocks is dominated by the matrix resistivity, while the resistivity of sedimentary rocks is dominated by the porosity, water saturation, and the resistivity of the pore water. The gas hydrate resistivity here refers to the bulk resistivity of the sediment containing gas hydrates found through geophysical exploration, not the value range of pure gas hydrates (this figure was adapted from [33]).

The generation of gas hydrates determines the resistivity of the final gas hydrate occurrence. Before gas is produced, the marine sediments are filled with brine and have a low bulk resistivity. The resistivity value is determined by the porosity, ion concentration, and mobilities [34]. The ion concentration and mobilities are usually stable in marine sediments, which makes the resistivity primarily determined by porosity and water saturation. While gas is being generated in the pore space, it solidifies under pressure and begins to push out the brine, thereby blocking the pore connections. The formation process causes the resistivity to first decrease and then increase, which has been validated in experiments [34]. To detect a resistive body in a conductive environment, we can use EM methods, which have been used for hydrocarbon exploration.

Figure 2 shows a model that illustrates the principle of EM measurements. An EM field is emitted by the source (red star) and registered by the receiver (red triangle). The diffusive electromagnetic field propagates in all directions; the four main paths are indicated by the colored arrows: the direct field (pink arrows) from the source to the receiver, the direct air wave contribution (black arrows), the direct ground wave (the green arrows), and the contribution from the reservoir (the grey arrows). The electric field at the receiver that has had paths through the reservoir provides the only part of the data that contains information

about the reservoir. The data is used to obtain information about the reservoir such as its shape, depth, and resistivity.

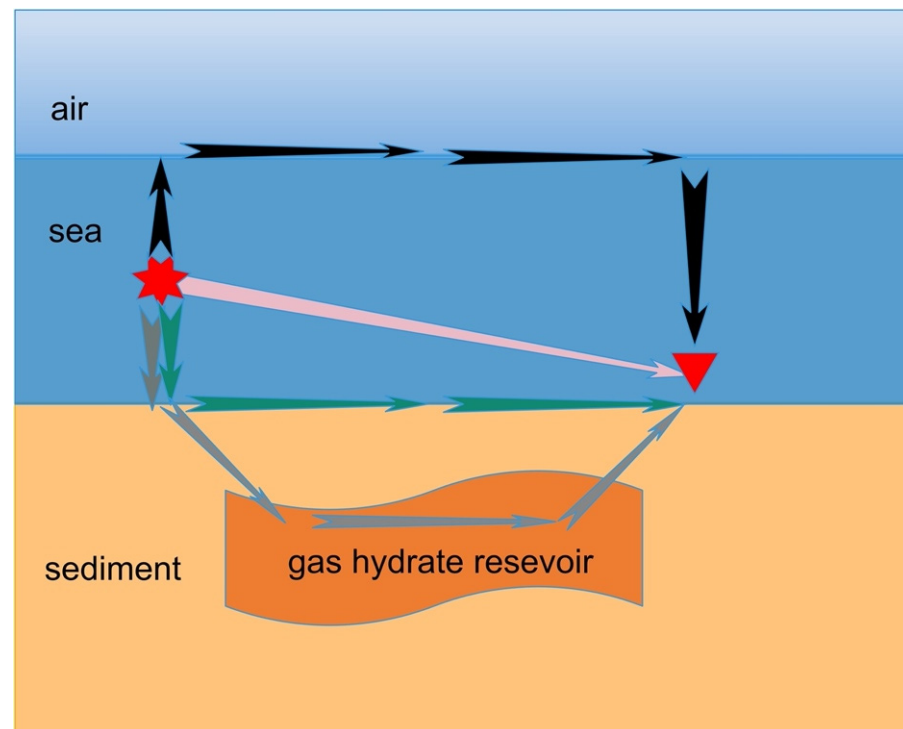


Figure 2. An illustration of diffusive electromagnetic field paths through the model for the given configuration. The gas hydrate reservoir is embedded in the sediments. The red star and triangle represent the source and the receiver, respectively. The arrows indicate the main propagation paths of EM field: direct field (pink), direct airwave contribution (black), direct ground wave (green), and the direct contribution from the reservoir (grey).

A 2D sensitivity analysis was performed on the difference between the gas-hydrate-filled sediments and the surrounding sediments as a function of the resistivity contrast, burial depth, and area as variables [35]. The results showed the position of the gas hydrate well when the thickness of the target was 100 m and the resistivity ratio of gas-hydrate-filled sediment over water-filled sediment was 6. However, the inversion results were not satisfactory when the resistivity ratio decreased to a lower value than 6. If, e.g., the resistivity of the overburden was $1 \Omega\text{m}$, and the resistivity of the reservoir was larger than $6 \Omega\text{m}$, the reservoir could be detected [35]. The sensitivity of the method was computed in forward modeling [36,37]; that is, we could still obtain a good resolution when the product of the resistivity difference between the anomalous body and the surrounding seawater and the thickness of the model was no less than 600.

3. Acquisition Methods

We now turn to the choice of the acquisition configuration for the target depth, the desired information, the different types of transmitters, and the source and receiver configuration. In this section, we restrict ourselves to acquisition configurations that have been used specifically for the exploration of natural gas hydrates [38]. We divided the configurations into two types. The first type is the stationary receiver configuration, in which the source can be towed or be stationary on the seafloor. The second type is the towed-streamer CSEM in which both the source and receivers are towed. This includes the seafloor-towed and deep-towed configurations.

3.1. Towed Source and Seafloor Receiver Configuration (Conventional Configuration)

The configuration with seafloor receivers and a towed source was introduced to detect large resistive bodies in a marine environment [39]. This configuration has been changed for gas hydrate detection. According to Constable [28], the dipole transmitter with two electrodes at the end is towed about 30–100 m above the seafloor, while individual electric and magnetic field receivers are placed on the seafloor (see Figure 3). The electrodes consist of two copper cylinders to generate the electromagnetic field. A real-time monitoring system tracks the position, vibration, and temperature of the transmitter. The source time signature can be a sinusoidal signal, a square wave, an optimized waveform, or a pseudorandom binary sequence. The current strength varies between 100 A to 1 kA. The receiver measures the entire magnetic field vector and the two horizontal electric field components. This configuration was used successfully for gas hydrate exploration in several places such as Oregon, USA [40]; the Northeast Cascadia margin [41,42]; the Western Black Sea, North Atlantic [43]; and the mid-Norwegian continental margin [26,44]. This configuration has some limitations such as high operational costs, large navigational errors relative to towed receivers, saturation of the electric field sensors at short offsets, and gaps in data coverage between widely spaced receivers [26,45].

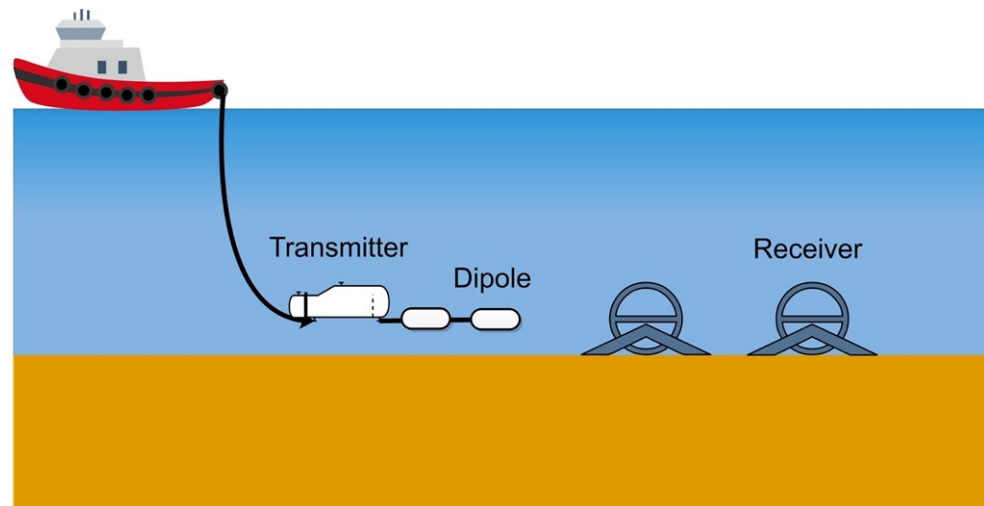


Figure 3. The towed source and seafloor receiver configuration.

3.2. Stationary Configuration

We will now examine two stationary configurations that have been developed. One is the Sputnik configuration, which was developed to overcome the experimental limitation of single-transmitter polarization by using two orthogonal electric dipoles as the source [20]. The other is the NEPTUNE configuration with instrument connections to a platform for long-term monitoring of resistivity changes [46].

In most previous Sputnik operations, measurements were carried out at offsets between 100 m to 1000 m. This configuration is sketched in Figure 4 [20]. The receivers can be used in passive (MT) and active (CSEM) modes. The transmitter has four arms as electrodes that can be folded. When it is operated after deployment of the receivers, the arms are mechanically folded, after which it is dropped with a winch. When it reaches the seafloor, the arms unfold to horizontal electric dipoles. After that, the transmitter can be used to generate any source time signature for each of the two polarizations in chronological order. The configuration was used with a square wave for 2 min in the Danube paleo-delta in the western Black Sea to search for gas hydrate reservoirs. In that survey, data at short offsets of less than 250 m were collected [20].

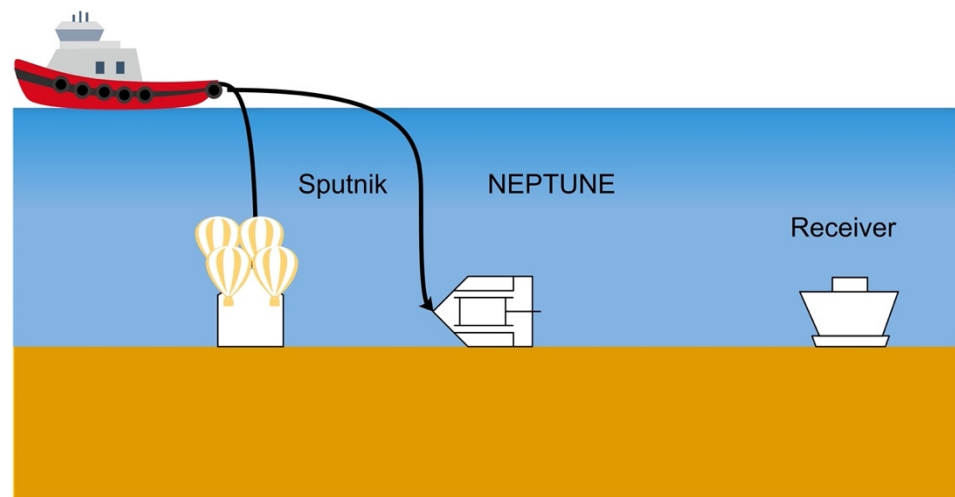


Figure 4. Stationary configurations of Sputnik (from [20]) and NEPTUNE (from [46]).

The North East Pacific Time-Integrated Undersea Networked Experiments (NEPTUNE) observatory led to the NEPTUNE configuration. It was developed to provide a platform for long-term studies. It consists of an electric current dipole as a source and individual receivers to measure only the electric field. All the power and data communication are connected to the platform. It is also a transient dipole–dipole time-domain EM system. During the launching operations, this configuration is placed with the help of an underwater remotely operated vehicle (ROV). The total length of the receiver string is 1 km and the receivers are spread equally along the array at 200 m intervals. The instrument is powered by the NEPTUNE observatory. The communication between transmitter and receivers is relayed by the NEPTUNE network to the seafloor junction box. Data can be collected remotely by connecting to the configurations through the web [46]. This configuration was used for weekly collection of data in October 2010. The results showed that the configuration could detect small changes in the resistive structure of gas hydrates [47].

3.3. Seafloor-Towed Single-Line Configuration

Navigational errors in transmitter positions contribute to large errors in CSEM data at short source–receiver offsets (compared with the stationary receiver). To connect the transmitter and the receiver together, the single-line configuration, shown in Figure 5, is easy to operate during fieldwork with little chances of the receiver being lost. The single-line configuration with an electric or a magnetic source can reduce navigational errors [48].

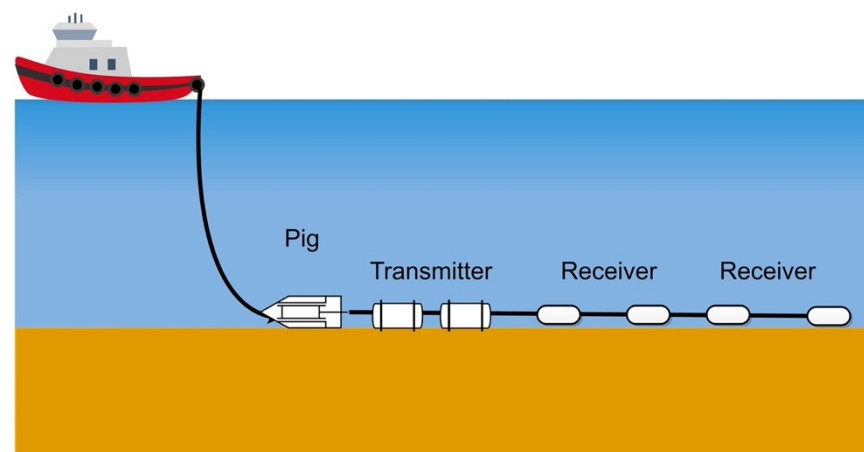


Figure 5. The single-line configuration.

The electric dipole–dipole configuration (first from University of Toronto [49,50]) was used to examine the properties of gas hydrate deposits in the Cascadia margin off Canada's west coast. The source dipole length was not reported, but the measurements were taken with 377 m and 493 m offsets. Because the resistivity was remarkably uniform over the area, the resistivity map allowed for hydrate content estimation, and the presence of hydrate was predicted where no visible BSR signal was present in the seismic data.

At the same site, this configuration was used in 2005 with an electric dipole transmitter 126 m in length and two receivers 15 m in length with an offset of 174 m and 192 m, respectively, and with a variable offset depending on the depth of interest. The signal from the transmitter was a square wave with a peak-to-peak amplitude of 20 A and a period of 6.6 s. All the instruments were bottom-towed on the seafloor. This system was used to collect transient and frequency domain data [14,51]. It was tested to reveal the electrical signature of the vent field and the seismic blank zones in the Cascadia margin in close vicinity to ODP Site 889 [51].

In 2010, the electric dipole–dipole configuration was used in the time domain in the Southern Central Hikurangi Margin off the east coast of New Zealand's North Island with offsets of 172 m and 275 m. The signal of the transmitter was a square wave with a period of 3.36 s and bidirectional amplitude of ± 5 A [52], which was limited by the gauge of the coaxial cable [53]. The system was flexible enough to place various receivers at different offsets in surveys. For example, the transmitting dipole (108 m) and up to five inline receiver dipoles (150 m to 850 m) of lengths between 15 m and 20 m were used in the Danube deep-sea fan in the Black Sea [54].

Due to the noise in electric dipole receivers when moving, magnetic dipole source and receivers are primarily used to permit the source to move continuously while making measurements. The inline magnetic dipole–dipole configuration was deployed by the Geological Survey of Canada [55]. Similar to the electric dipole, the magnetic dipole source excited both poloidal and toroidal modes of current flows with three receivers spaced 4 m, 13 m, and 40 m behind. The rig was pulled along the seafloor at speeds of 1–2 knots [56]. The magnetic single line was used in the Mississippi Canyon of the Gulf of Mexico [56].

3.4. Deep-Towed Single-Line Configuration (Vulcan)

In order to lower the operational costs and reduce logistic efforts, the fixed-offset SUESI with the Vulcan CSEM system (from Scripps Institution) helps to mitigate some of the limitations and allows for the continuous recording of usable data [26].

The array is suspended in the water column as sketched in Figure 6 or towed in contact with a relatively flat seafloor. In contrast to the conventional configuration, the data stored in this configuration are synchronized between the transmitter and the receiver with a precision clock [52]. This configuration has been used with a towed transmitter at 50 m to 100 m above the seafloor with receivers at fixed offsets of 150, 250, 350, and 450 m and with a total length of 500 to 1200 m [52]. Due to the fixed offset, this configuration is suitable for gas hydrate imaging [52,57]. The used frequencies are 1.5, 3.5, and 6.5 Hz. Frequency-domain data is collected in terms of the amplitude and phase and inverted to obtain the average bulk resistivity distribution of the seafloor. When used in a seafloor-towed array, this configuration uses a pig at the head of the transmitter dipole so that it tows in contact with the seafloor. However, this adds the risk of sensor damage when the seafloor is not flat enough.

The deep-towed source is the same as the conventional configuration, but with the receivers behind it can cover larger survey areas using comparable ship time. In addition to the inline field data, the Vulcan vertical field data include broadside data and provide unique constraints on lateral structures [26]. This configuration was used for hydrate exploration in the Gulf of Mexico [52,53], offshore of Japan, in the San Diego Trough survey [52], in the Del Mar Seep [58], in the California Borderlands [59], and in the mid-Norwegian continental margin [26].

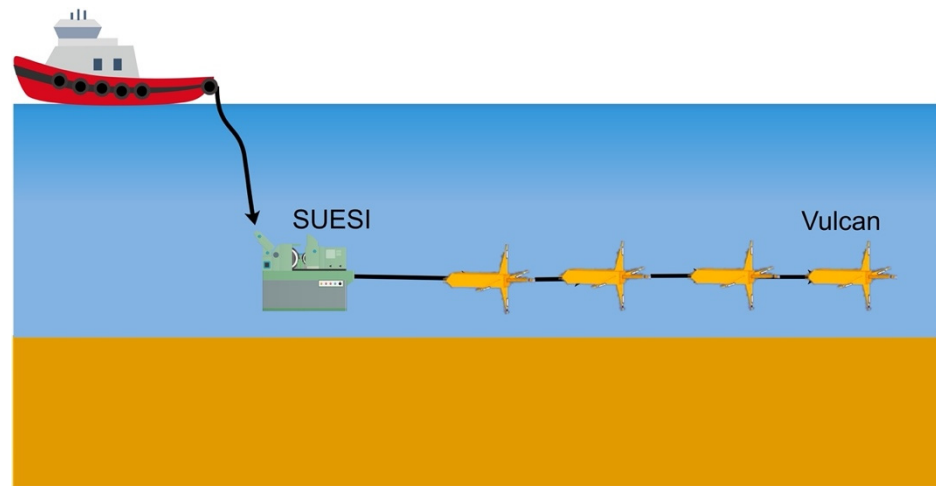


Figure 6. The SUESI with Vulcan configuration (adapted from [26]).

4. Numerical Examples for Comparison of Acquisition Configurations

For the numerical example, we took a 1000 m thick water layer with a resistivity of $0.3 \Omega\text{m}$. The top of the reservoir was buried 200 m below the seafloor. The reservoir was 700 m long, 700 m wide, and 100 m thick with a resistivity of $50 \Omega\text{m}$. We used an inline horizontal electric dipole with a source frequency of 6 Hz. At this frequency, the top of the reservoir was at approximately one skin depth below the seafloor. For acquisition geometries with stationary receivers (shown in the top row of Figure 7), we used source positions from -750 m to 750 m with a 30 m interval right over the middle of the reservoir. Stationary receivers were displaced 15 m in the inline direction from the stationary source. The towed source in this configuration was 50 m above the seafloor. For the towed-receiver configurations (bottom row), the receivers had offsets of 720 m, 960 m, 1200 m, and 1440 m. When they were towed in the sea, they were 50 m above seafloor. The other configuration used towed sources and receivers on the seafloor.

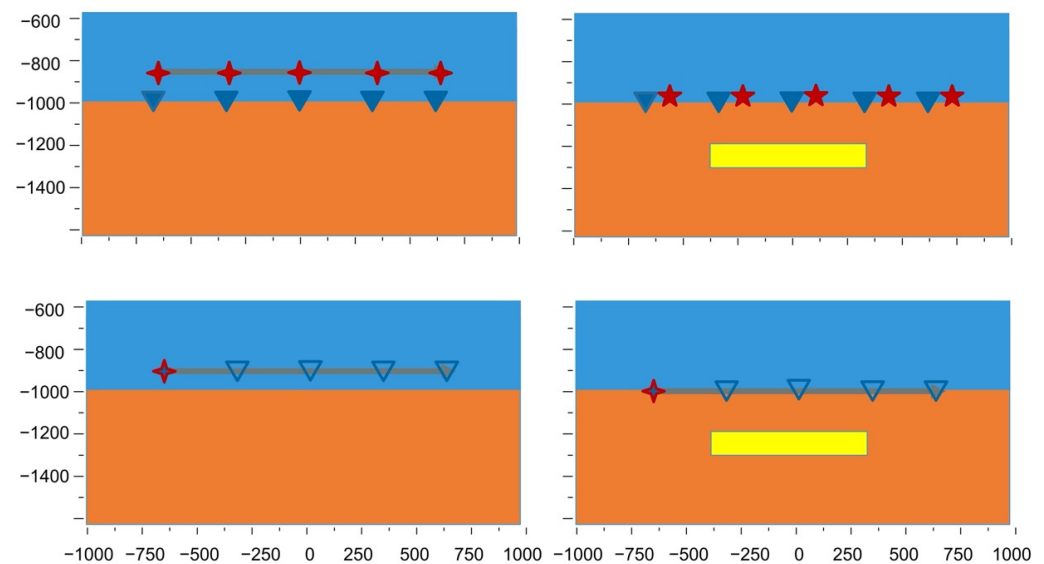


Figure 7. The background model with sea and overburden (blue and orange, left column) and model with embedded gas hydrate reservoir (yellow, right column); with stationary-receiver configuration with the seafloor receivers (closed triangles, top row); and towed-receiver configuration with fixed offset of 720 m, 960 m, 1200 m and 1440 m (open triangles, bottom row). The towed line is indicated by the grey line. The stationary source is indicated by the five-point red star. The towed source was 50 m above the seafloor (four-point star).

We used the normalized amplitude difference (NAD) to evaluate the changes:

$$\text{normalized amplitude difference} = \frac{|E_{withreservoir} - E_{basemodel}|}{|E_{basemodel}|} \quad (2)$$

Figure 8 shows the NAD in the electric field with and without the gas hydrate present. The top row show the results as a function of the source and receiver locations along the acquisition line for receivers in the stationary configurations with the source 50 m above the seafloor (left) and at the seafloor (right). The bottom row shows the results as a function of the source location and receiver offset for receivers in the moving configurations with the source 50 m above the seafloor (left) and at the seafloor (right). The edges of the reservoir are indicated in the receiver positions by the vertical white dotted lines. The white dash-dotted lines indicate the horizontal locations at one burial depth away from the edges of the reservoir. The horizontal white line indicates the left edge of the reservoir in the source position. The red line indicates the first offset in the moving configurations. The white solid line is the 0.25 contour line. If the NAD was larger than 0.25, we had full confidence that the reservoir was detectable as containing gas hydrates. The maximum response of the gas hydrate existence was four times higher than the response of the model without the reservoir.

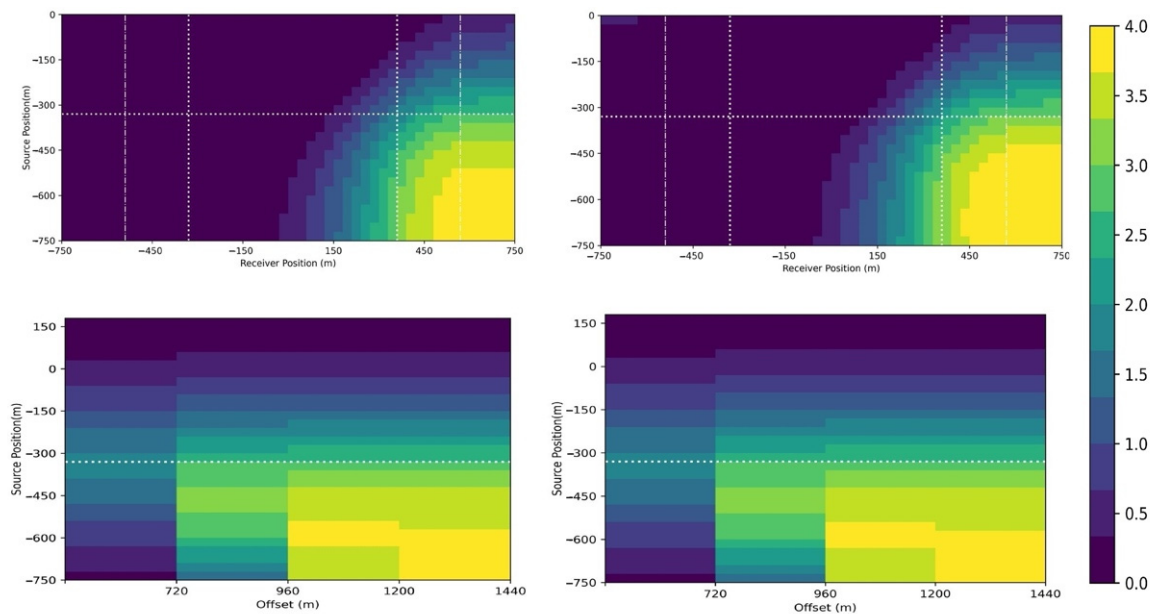


Figure 8. The NAD in the inline electric fields with and without the reservoir for the stationary (top row) and moving (bottom row) receiver configurations and with the source 50 m above (left column) and on (right column) the seafloor. The *x*-axis is the position of receiver or the offset, and the *y*-axis is the source position. Because the geometry was symmetric, we only show the source positions from −750 m to 0 m in the top row, while we show it for the source up to 150 m in the bottom row. The white dotted lines indicate the edges of the reservoir in receiver position (vertical lines) and source position (horizontal line). The white dash-dotted lines indicate the horizontal locations one burial depth away from the edges of the reservoir. The red line indicates the first offset (720 m) in the moving receiver configurations. The white solid line marks the 0.25 contour. The red line shown the fixed offset acquisition position.

The NAD had the same maximum value in the stationary and moving receiver configurations. The choice of offset was important. Considering the 700 m length of the reservoir, the red line in Figure 8 shows that the presence of gas hydrates could be seen only for offsets larger than 700 m. Once we found an optimal range of offsets, having four receivers was enough to show the existence of the gas hydrate reservoir in this example. The results for a source on or 50 m above the seafloor were not so different from each other. The main

effect was that the electric field amplitude dropped by 60%, but the NAD changed by 12%. Placing the source at 50 m above the seafloor mostly limited the maximum offset that could be used (see Figure 9). A cutoff amplitude of $1e-13$ V/m for the electric field was used to draw Figure 8; we assumed this amplitude was detectable. This meant that for the stationary configuration, all receivers were available to detect the presence of the gas-hydrate-filled reservoir. If we increased the frequency by a factor of four to 24 Hz, the maximum amplitude of the normalized difference in the electric field in the absence and presence of the gas hydrate reservoir was four times higher than at 6 Hz. The maximum could be more than 10 times higher with a lower cut-off amplitude. For our choice, not all receivers could be used at this higher frequency because of the larger attenuation that can be seen in Figure 10, which shows the results for the source on the seafloor.

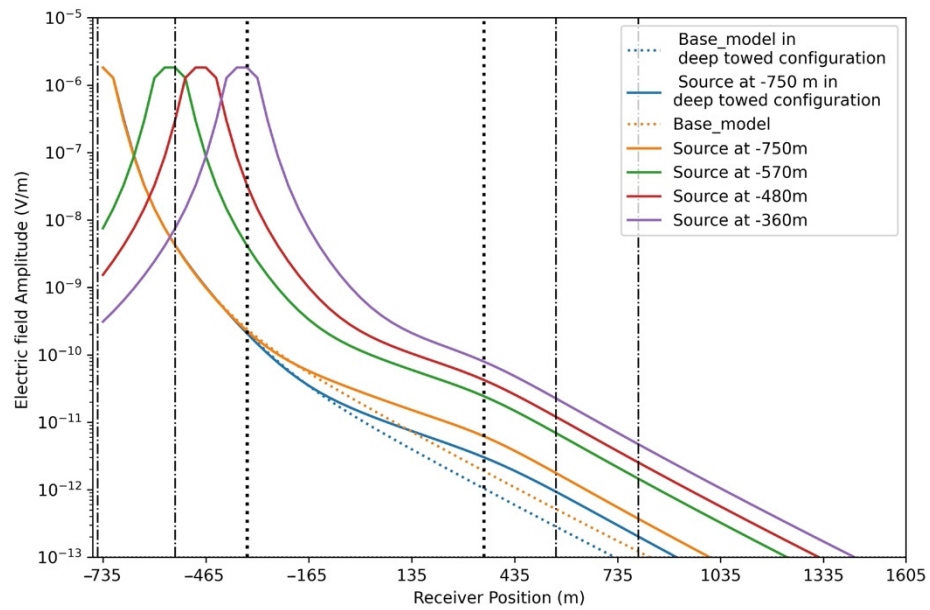


Figure 9. Electric field amplitude for stationary-receiver configurations (colored lines) and deep-towed configuration (blue line). The base model without the reservoir (dashed line) is compared with the model with the reservoir from the same source.

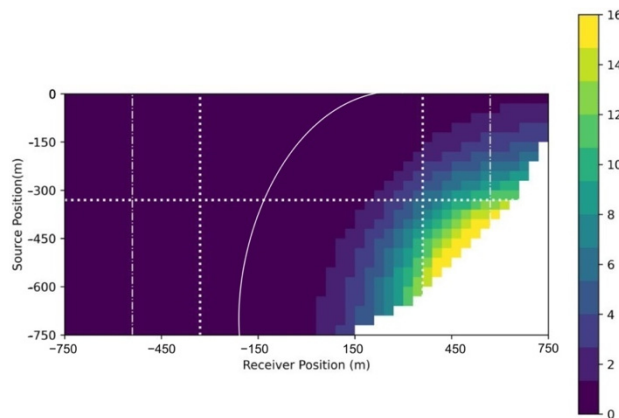


Figure 10. Amplitude of the normalized difference in the electric field at 24 Hz.

Figure 11 shows the amplitude of the NAD in the electric field for individual 6 Hz sources as a function of the receiver location. The blue curve shows the results for the source located approximately two burial depths to the left of the reservoir. The presence of the reservoir can be seen in receivers beyond the right edge of reservoir. The NAD increased to a maximum value at almost one burial depth to the right of the right edge of the reservoir. For this source, the NAD dropped quickly for receivers beyond one burial

depth to the right edge of the reservoir. We concluded that for this source, the information on the presence of the gas hydrate reservoir was slowly lost for receivers more than two burial depths to the right of the right edge of the reservoir. When the source was between one burial depth left of the left edge of the reservoir and the left edge, the NAD showed an increase from the receivers that were two times the burial depth to the right of the source and reached a peak almost at the one burial depth to the right of the right edge and then become constant. For all the sources in this range, the normalized difference amplitude for the receivers showed the same behavior until the source was located right above the left edge. In that case, the NAD increased toward a constant value. A constant value in the NAD meant that the decay for those source–receiver pairs with and without the gas hydrate present was the same. This corresponded to the results presented by Constable [60].

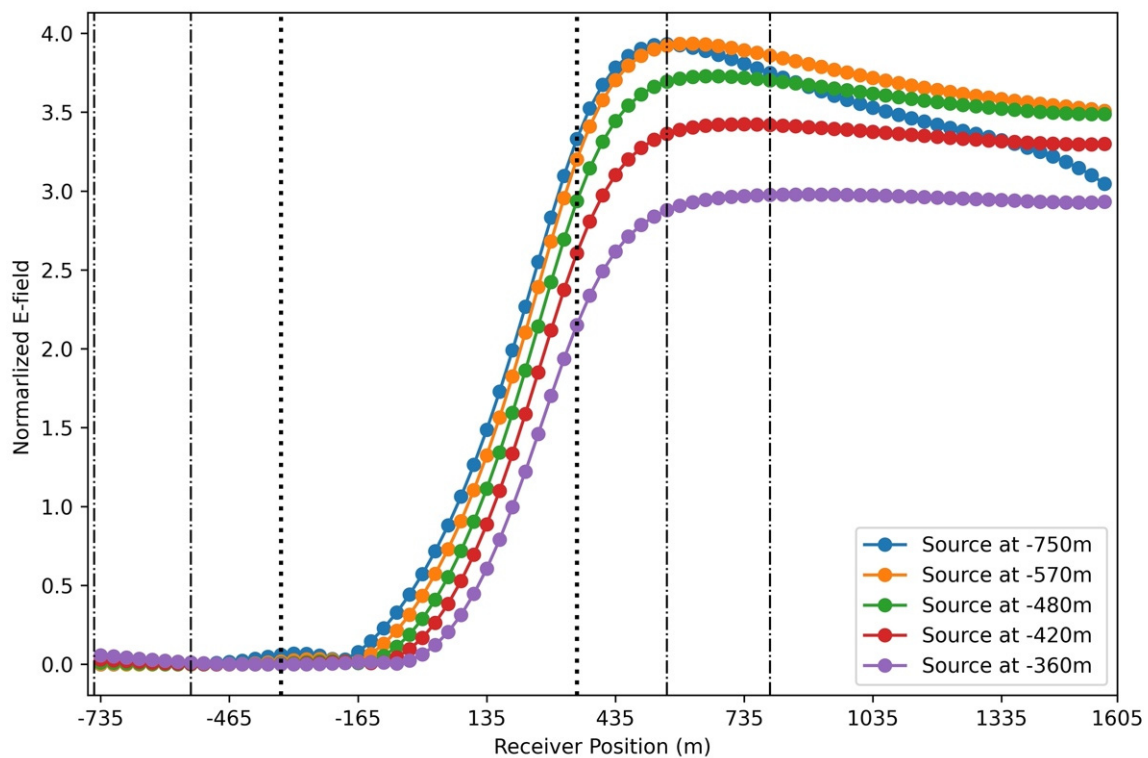


Figure 11. NAD of the inline electric field with and without the reservoir.

The results allowed us to determine the horizontal boundaries of the reservoir. The source for which the receivers showed a normalized difference amplitude curve that had a large constant value for a large offset and had the highest peak value was located at one burial depth to the left from the left edge of the reservoir. Assuming that we knew the burial depth from seismic data analysis, this determined the location of the left edge of the reservoir. The location of that highest peak value was almost at one burial depth to the right of the right edge. This determined the right edge of the reservoir.

5. How to Choose a Configuration

To decide which configuration to use to collect field data, one needs to consider the expected target dimensions, depth location, geophysical parameter contrasts, required information, operational convenience, required navigation accuracy, source time signature, towing speed, survey repeatability, noise level, and cost. Table 1 provides some key parameters of the four configurations. The important aspects derived from these acquisition configurations can be summarized as follows.

Table 1. Overview of acquisition information.

Aspect	Conventional Configuration	Stationary	Seafloor-Towed Single Line	Deep-Towed Single Line
Water depth	Any	>1000 m	Shallow water (<~500 m)	>1000 m
Detection depth(m)	0–4000	0–1000	0–1000	0–1000
Source time signature	Variable square wave	Variable wave	Variable square wave	Square wave Transient
Receiver	E + M	E + M	E/M	E (+M)
Operation step	Sinking the receiver Towing the transmitter	Sinking receiver and placing the transmitter	Tow one line	Tow one line
Operation of ship (speed in knots)	About 1.5–2	No	Above 4.5	1.5–2
Data communication	Asynchronous	Asynchronous (Sputnik), synchronous	Synchronous	Synchronous
Offset geometry	Flexible	Flexible	Fixed	Fixed
Risks during operation	Lost receiver	Lost transmitter and receiver	Low risk	Line stuck in sea floor

1. Acquisition construction: for the stationary receivers, first all individual receivers are sunk to the seafloor. Then the transmitter is deep towed by the ship or sunk to the desired location. The stationary receiver configurations can record the inline and broad field; for the towed receivers, the ship can tow all instruments, but only the inline electric field can be recorded.
2. Distance above the seafloor: the distance between the seafloor and the acquisition configuration affects the noise level. When the distance is small, such as in the stationary configuration, the results show better signal-to-noise ratios than when the source of conventional configuration is in the sea. The deep-towed configuration is the configuration with the largest distance to the seafloor compared with other configurations, and the detected noise levels are higher than in the other configurations [31,61].
3. Navigation accuracy: the orientation and location information of the receivers sunk to the seafloor in stationary configuration may not have the required accuracy in the deep sea. For the Sputnik configuration, the distances between the transmitter and the receiver can be measured directly at the seafloor. The towed-receiver configurations will reduce the position error. With all towed systems, the dynamic orientation and location information can be obtained with high accuracy, because more time is available to determine them. It is possible to work with four orientation-invariant data values that can be obtained from the measured data without knowing the orientation of the source currents and electric field receivers [62].
4. Towing speed: this is constrained by the towed line because if the speed is lower than 2 knots, the towed line tail may sink and be damaged when it touches the seafloor. Higher speeds improve acquisition time efficiency, but these limit the frequency bandwidth that can be used.
5. Offset: in the stationary-receiver configurations, the transmitter is located independent of the receivers and offers flexibility in offsets, such as the configuration used in Sputnik [20]. In the fixed-offset, single-line, and Vulcan configurations, the source-receiver geometry is fixed but can be flexibly combined with receivers with different offsets in each survey.
6. Data communication: data can be transmitted to the ship while it is being collected when there is a physical connection such as the in single-line and Vulcan configurations. If that connection does not exist, then power, ADCs, and memory cards are necessary in the instrument.
7. Costs: obviously, the application of CSEM in gas hydrate exploration must influence operational management decisions to be of value in commercial operations. The costs should be lower than the benefits that can be obtained from the CSEM data. Generally, the cost of a CSEM survey is governed by the required ship time, which depends

on several factors such as the water depth, acquisition area, and acquisition speed. Another aspect is the costs of the possible rescue or the possible loss of the instruments.

Based on the technical discussion above, we derived three steps that can be used to choose the most effective acquisition configuration to undertake a gas hydrate survey.

First, the survey accuracy depends on the water depth in which the potential gas hydrate target is present. This means that water depth is a key factor of influence, which can be seen in Table 1. In all water depths, constraining the receivers to the seafloor will lead to low magnetotelluric noise in the receiver compared with that for receivers floating in the seawater, which follows from the distance above the seafloor.

Second, the depth of the target gas hydrates is another constraint on the choice of the configuration. The survey line needs to have offsets of at least 2.5 times the target depth, which works well only if the extent of the target lateral is at least the required offset.

Third, the costs of the survey affects the choice of the configuration. According to the different operation configurations discussed, the efficiency of different configurations in operation steps and the ship speed are related to the costs of the survey. By considering the costs in discussion point 7 above, it can be determined whether a CSEM survey is likely to be successful for gas hydrate exploration, and if so, what the preferred configuration will be.

6. Applications of Measurement Configurations

CSEM has been a useful geophysical method to discriminate between high and low hydrocarbon saturation in a potential reservoir [31,50,63–66]. Many applications in natural gas hydrate detection have been published from, e.g., the North Sea [67,68], Taiwan [69], the Gulf of Mexico and Canada [70], the Danube Paleo-Delta [20], Norway [44], the South China Sea [71], and the Western Black Sea [54].

Table 2 shows several applications for gas hydrate exploration. We listed information related to the reservoir including gas hydrate occurrence, the depth of the sea, the burial depth below the seafloor, the hydrate saturation, which electromagnetic measurement configuration was used and whether it was used after drilling, and the resistivity of the hydrate-containing sediments. As can be seen in Table 2, seismic and electromagnetic surveys were carried out in all locations. Seismic surveys are the first geophysical method employed to determine the presence of gas hydrates. The drilling decision should be taken after joint interpretations of the seismic and CSEM data [38]. Only in two locations the electromagnetic surveys shown in Table 2 were done prior to drilling. For several applications for gas hydrate reservoirs, two CSEM configurations were used together.

Table 2. Geophysical exploration and gas hydrate information at several sites.

Place	Water Depth (m)	Drilling	EM Configuration	Resistivity of Hydrate-Containing Sediment (Ωm)	Gas Hydrate Depth (MBSF)	Hydrate Saturation (%)
North Sea	150	Before EM	Vulcan Conventional configuration [68]	1.9	150	40 and 50
New Zealand's North Island	1000–1100	After EM	Single line (E)	10 (apparent resistivity)	40–80	Variable with porosity (15.7–50) [6]
Taiwan	1060–1080	Before EM	Single line (M) [69], Sputnik [66]	1.0 ~2.0 (apparent resistivity)	Area A, B, C shallow (<30)	16 (in the shallow sediments)
Malaysia	>1219	Before EM	Conventional configuration Single line (M) [56],	15	100–400	10
Gulf of Mexico	1300	After EM	conventional configuration, Vulcan [53]	0.1–1.0	18 ~ 78	—
Danube Paleo-Delta	1500	Before EM	Single line (M) [54], Sputnik [20]	20–30 (first layer) 15–30	60–120	23 (by estimate according to Archie's law)

1. Vulcan + conventional configuration

These two configurations were used in the San Diego Trough Test in March 2015 [52] and in the North Sea [67,68]. For the San Diego Trough Test, the Vulcan was originally designed to be used in conjunction with the conventional configuration to help constrain near-seafloor conductivity structure between the instruments. When comparing the two configurations, it was found that the Vulcan saved ship time, which reduced the cost of the exploration. The Vulcan was much less demanding on the navigation system than the conventional configuration. The results showed that with the Vulcan data, a much better resolution of the seafloor resistivity structure could be obtained than when using only seafloor receivers. It was suggested that depth sensitivity may have been comparable to the maximum source–receiver separation, which was better than one would expect for the conventional configuration.

2. Seafloor-towed single line + Sputnik

These two configurations were used together in Taiwan and the Danube Paleo-Delta as shown in Table 2. The Danube Paleo-Delta profile data from the single-line seafloor-towed system and from the Sputnik were inverted separately and the inversion results compared. The Sputnik results showed visible changes in adjacent cells and seemed to have better resolved the effects of anisotropy. The Sputnik consisted of 12 ocean-bottom electromagnetic receivers and 81 transmitter locations. Due to this reduced coverage (compared with the towed line), the resistivity model was less well resolved and some visible features must be potential artifacts.

3. Seafloor-towed single line (E) + NEPTUNE

In the Cascadia Margin Canada, gas hydrates were detected using the seafloor-towed single-line configuration together with seismic and drilling data [51]. The NEPTUNE survey was an opportunity to gain experience with the CSEM instrumentation and deployment procedure to improve the design of the NEPTUNE CSEM array [46]. The NEPTUNE data were used to show changes in the seafloor resistivity by plotting the stacked seafloor response for the different dates in the same graph.

We now focus on the different goals of the CSEM method. The CSEM method was primarily used as a complementary technique as part of geophysical exploration to provide information on the resistivity of the hydrate reservoirs. The additional contributions enabled by the CSEM data were the determination of the upper boundary of the hydrate stability zone [72] and the profile distribution of gas hydrates in shallow sediments [73]. Finally, CSEM was used in a time-lapse survey to monitor the long-term resistivity changes [46].

To provide an estimate of the top boundary of a gas hydrate zone in the Japan Sea, Goto et al. performed a CSEM survey that allowed estimation of the precise depth and the resistivity values of the gas hydrate zone [72,74]. In the Pelotas Basin offshore of Brazil [75] a CSEM survey was used to map the resistivity and predict possible hydrate occurrence. This was overlooked due to the lack of a clear seismic or multi-beam backscatter signature obtained from 2D seismic, sub-bottom profiler, and multi-beam bathymetry data.

CSEM data can be an excellent discriminator between high and low hydrocarbon saturation [51], which helps to estimate the total volume of hydrates in place. This can be converted to a total available gas estimate and a further quantification of the gas hydrate concentration [66]. In Malaysia, a CSEM survey was carried out after seismic and logging surveys that provided an estimate of the resistivity distribution of the gas hydrates. Even though the seismic data had pointed out the existence of gas hydrates, the total mass of the hydrates were evaluated using the resistivity of gas hydrate reservoir [76]. CSEM detection needs to be improved to improve safe commercial production [77]. CSEM exploration was carried out in Taiwan with an aim to provide electrical resistivity information on gas hydrates in shallow sediments. This should help in reaching a better understanding of the upper boundary, which was still an uncertainty from the seismic results [69,78–80]. In this area, two kinds of CSEM acquisition configurations were reported to collect resistivity data. In the Danube Paleo-Delta survey, the CSEM survey offered the opportunity to provide

areawide volume estimates of gas hydrates and free gas saturations. To discriminate between free gas and gas hydrates, joint seismic and EM inversion was performed with structural constraints to provide more accurate saturation estimates than those provided by either seismic or electromagnetic inversions alone [20,54].

Shallow gas hydrates can be a hazard for drilling to deeper targets because the gas hydrates can be released as free gas and flow into the well bore unexpectedly. The CSEM method is well suited to evaluate the risks and improve cost-effectiveness for another exploration drilling and provided good suggestions for the drilling position for safe commercial production. Weitemeyer et al. conducted a CSEM exploration survey in Hydrate Ridge, Oregon, USA after seismic and logging surveys [65]. This provided a direct measurement of the bulk hydrate concentration and a measurement of the hydrate distribution based on the log data. Including CSEM data in the analysis provided a better estimate of the total volume than could be obtained with seismic and log data alone. It also enabled an estimate of the hydrate concentration in locations where the sediments were altered and disturbed compared with the location where the log data were obtained [40].

CSEM data can help in geological modeling to improve the understanding of the gas hydrate formation process. CSEM has found a comprehensive application in the understanding of hydrate reservoir formation as reported in several studies [14,81–86]. In the Gulf of Mexico, seismic and CSEM surveys were designed before drilling, which led to improved detection efficiency [56]. The seismic and CSEM surveys were completed with side-scan sonar, coring, heat-flow measurements, and drilling after CSEM. The CSEM data were successfully used in mapping the flow of the methane transport in shallow sediments. In this case, although there was no obvious sign of higher resistivity caused by the presence of gas hydrates, the logging after CSEM suggested that the CSEM data had resulted in proper resistivity estimates and that the effects on the resistivity of the hydrates were masked. CSEM has been carried out to aid in geological interpretation in relation to gas hydrate occurrences to map the electrical nature of gas-filled and gas-hydrate-filled sediments that were associated with, e.g., seeps. Where the survey was performed together with seismic, geochemical, and heat-flow measurements, the CSEM survey was developed without a drilling plan. This occurred offshore of the east coast of New Zealand along the Hikurangi Margin. In this case, the CSEM data predicted the high-resistivity zone in remarkable agreement with the location of the gas hydrate accumulation. All these measurements suggested that the reason for the stability of gas hydrates and their formation is related to the rising transport of fluid methane [87]. CSEM results showed anomalous resistivity zones that were coincident with the location of two gas-seep sites. A layer of concentrated gas hydrates within the uppermost 100 m below the seafloor was verified by anomalous resistivity [14].

For gas hydrate monitoring, the NEPTUNE observatory was used to monitor small resistivity changes in the long term [46]. Changes in porosity and gas hydrate saturation were difficult to measure based on CSEM data alone. This could be improved by using seismic velocity data and drilling data [38].

7. Conclusions

We have shown the two kinds of EM configurations that are being applied for gas hydrate exploration. These use either stationary receivers on the seafloor or towed receivers. With stationary receivers, a towed source or a source placed on the seafloor can be used. For the towed receivers, the source is towed in line with the receivers. Our numerical results showed that all configurations could be used to detect a 700 m long gas hydrate reservoir buried 200 m below the seafloor in a 1 km deep sea. In addition, the stationary configuration provides data that can be used to estimate the horizontal boundaries of the resistive part of the reservoir when the burial depth is known from seismic data. Detectability is directly related to skin depth. We used a minimum electric field amplitude of 0.1 nV/m to show that when the top of the reservoir was two skin depths below the seafloor, the maximum

amplitude of the normalized difference was four times higher than when the top was at one skin depth below the seafloor.

We suggest a workflow that considers three crucial aspects: the water depth, target depth and lateral extent, and survey cost. This allows for choosing the most suitable CSEM acquisition configuration for a given scenario. The discussed configurations have all been applied in gas hydrate surveys after seismic data were collected. Based on resistivity contrasts found in the field, the CSEM method can be used to reduce the uncertainty in the estimates regarding the presence and total volume of gas hydrates. To reduce the risk of drilling a non-commercial play, an accurate estimation of the total volume and phase of the hydrate is crucial, and CSEM can play an important role in this. Our results can help to decide whether to employ CSEM for gas hydrate exploration and how to choose an efficient and effective acquisition setup.

Author Contributions: Conceptualization, H.L., E.S., D.W. and Y.L.; writing—original draft preparation, numerical computations, figures, Y.L.; writing—review and editing, all authors. All authors have read and agreed to the published version of the manuscript.

Funding: This research was funded by the China Scholarship Council (grant number 202008110117) and the China Geological Survey (grant number DD20190234). The APC was funded by Delft University of Technology.

Conflicts of Interest: The authors declare no conflict of interest.

References

1. Ma, Q.L.; Chen, G.J.; Ma, C.F.; Zhang, L.W. Study of vapor-hydrate two-phase equilibria. *Fluid Phase Equilibria* **2008**, *265*, 84–93. [[CrossRef](#)]
2. Yu, Y.; ZHANG, X.-w.; Liu, J.-W.; Lee, Y.; Li, X. Natural gas hydrate resources and hydrate technologies: A review and analysis of the associated energy and global warming challenges. *Energy Environ. Sci.* **2021**, *14*, 5611–5668. [[CrossRef](#)]
3. Sloan, E.D., Jr. Fundamental principles and applications of natural gas hydrates. *Nature* **2003**, *426*, 353–359. [[CrossRef](#)] [[PubMed](#)]
4. Hassanpouryouzband, A.; Joonaki, E.; Farahani, M.V.; Takeya, S.; Ruppel, C.; Yang, J.; English, N.J.; Schicks, J.M.; Edlmann, K.; Mehrabian, H. Gas hydrates in sustainable chemistry. *Chem. Soc. Rev.* **2020**, *49*, 5225–5309. [[CrossRef](#)] [[PubMed](#)]
5. Ghosh, R.; Ojha, M. Amount of gas hydrate estimated from rock physics analysis based on morphology and intrinsic anisotropy in area B, Krishna Godavari offshore basin, expedition NGHP-02. *Mar. Pet. Geol.* **2021**, *124*, 104856. [[CrossRef](#)]
6. Milkov, A.V. Global estimates of hydrate-bound gas in marine sediments: How much is really out there? *Earth Sci. Rev.* **2004**, *66*, 183–197. [[CrossRef](#)]
7. Farahani, M.V.; Hassanpouryouzband, A.; Yang, J.; Tohidi, B. Insights into the climate-driven evolution of gas hydrate-bearing permafrost sediments: Implications for prediction of environmental impacts and security of energy in cold regions. *RSC Adv.* **2021**, *11*, 14334–14346. [[CrossRef](#)]
8. Wang, F.; Ma, R.; Xiao, S.; English, N.J.; He, J.; Zhang, Z. Anti-gas hydrate surfaces: Perspectives, progress and prospects. *J. Mater. Chem. A* **2022**, *10*, 379–406. [[CrossRef](#)]
9. Du Frane, W.L.; Stern, L.A.; Weitemeyer, K.A.; Constable, S.; Pinkston, J.C.; Roberts, J.J. Electrical properties of polycrystalline methane hydrate. *Geophys. Res. Lett.* **2011**, *38*, 47243. [[CrossRef](#)]
10. Waite, W.F.; Santamarina, J.C.; Cortes, D.D.; Dugan, B.; Espinoza, D.N.; Germaine, J.; Jang, J.; Jung, J.W.; Kneafsey, T.J.; Shin, H.; et al. Physical Properties of Hydrate-Bearing Sediments. *Rev. Geophys.* **2009**, *47*, RG4003. [[CrossRef](#)]
11. Spangenberg, E.; Kulenkampff, J. Influence of methane hydrate content on electrical sediment properties. *Geophys. Res. Lett.* **2006**, *33*, L24315. [[CrossRef](#)]
12. Lu, S.; McMechan, G.A. Estimation of gas hydrate and free gas saturation, concentration, and distribution from seismic data. *Geophysics* **2002**, *67*, 582–593. [[CrossRef](#)]
13. Rajput, S.; Thakur, N.K. *Exploration of Gas Hydrates*; Springer: Berlin/Heidelberg, Germany, 2011; Volume 58, p. 281.
14. Schwalenberg, K.; Haeckel, M.; Poort, J.; Jegen, M. Evaluation of gas hydrate deposits in an active seep area using marine controlled source electromagnetics: Results from Opouawe Bank, Hikurangi Margin, New Zealand. *Mar. Geol.* **2010**, *272*, 79–88. [[CrossRef](#)]
15. Riedel, M.; Eleanor, C. *Willoughby, and Satinder Chopra. Geophysical Characterization of Gas Hydrates*; Society of Exploration Geophysicists: Houston, TX, USA, 2010; Volume 14, p. 385.
16. Tamaki, M.; Fujimoto, A.; Boswell, R.; Collett, T.S. Geological reservoir characterization of a gas hydrate prospect associated with the Hydrate-01 stratigraphic test well, Alaska North Slope. *Energy Fuels* **2022**, *36*, 8128–8149. [[CrossRef](#)]
17. Ojha, M.; Sain, K. Quantification of gas hydrate and free gas in the Andaman offshore from downhole data. *Curr. Sci.* **2013**, *105*, 512–516.
18. Collett, T.; Lee, M. Well Log Characterization of Natural Gas-Hydrates. *Petrophysics* **2012**, *53*, 348–367.

19. Ojha, M.; Ghosh, R. Gas Hydrate Potential along the Eastern Continental Margin of India. *BMJ* **2021**, *2021*, 85.
20. Duan, S.; Hölz, S.; Dannowski, A.; Schwalenberg, K.; Jegen, M. Study on gas hydrate targets in the Danube Paleo-Delta with a dual polarization controlled-source electromagnetic system. *Mar. Pet. Geol.* **2021**, *134*, 105330. [[CrossRef](#)]
21. Edwards, N. Marine controlled source electromagnetics: Principles, methodologies, future commercial applications. *Surv. Geophys.* **2005**, *26*, 675–700. [[CrossRef](#)]
22. Archie, G.E. The electrical resistivity log as an aid in determining some reservoir characteristics. *Trans. AIME* **1942**, *146*, 54–62. [[CrossRef](#)]
23. Cook, A.E.; Waite, W.F. Archie's saturation exponent for natural gas hydrate in coarse-grained reservoirs. *J. Geophys. Res. Solid Earth* **2018**, *123*, 2069–2089. [[CrossRef](#)]
24. Shankar, U.; Riedel, M. Assessment of gas hydrate saturation in marine sediments from resistivity and compressional-wave velocity log measurements in the Mahanadi Basin, India. *Mar. Pet. Geol.* **2014**, *58*, 265–277. [[CrossRef](#)]
25. Riedel, M.; Collett, T.S.; Kim, H.-S.; Bahk, J.-J.; Kim, J.-H.; Ryu, B.-J.; Kim, G. Large-scale depositional characteristics of the Ulleung Basin and its impact on electrical resistivity and Archie-parameters for gas hydrate saturation estimates. *Mar. Pet. Geol.* **2013**, *47*, 222–235. [[CrossRef](#)]
26. Attias, E.; Weitemeyer, K.; Hölz, S.; Naif, S.; Minshull, T.A.; Best, A.I.; Haroon, A.; Jegen-Kulcsar, M.; Berndt, C. High-resolution resistivity imaging of marine gas hydrate structures by combined inversion of CSEM towed and ocean-bottom receiver data. *Geophys. J. Int.* **2018**, *214*, 1701–1714. [[CrossRef](#)]
27. Jana, S.; Ojha, M.; Sain, K.; Srivastava, S. An approach to estimate gas hydrate saturation from 3-D heterogeneous resistivity model: A study from Krishna-Godavari basin, Eastern Indian offshore. *Mar. Pet. Geol.* **2017**, *79*, 99–107. [[CrossRef](#)]
28. Constable, S. Ten years of marine CSEM for hydrocarbon exploration. *Geophysics* **2010**, *75*, A67–A81. [[CrossRef](#)]
29. Key, K. Marine Electromagnetic Studies of Seafloor Resources and Tectonics. *Surv. Geophys.* **2012**, *33*, 135–167. [[CrossRef](#)]
30. Constable, S. Review paper: Instrumentation for marine magnetotelluric and controlled source electromagnetic sounding. *Geophys. Prospect.* **2013**, *61*, 505–532. [[CrossRef](#)]
31. Constable, S.; Srnka, L.J. An introduction to marine controlled-source electromagnetic methods for hydrocarbon exploration. *Geophysics* **2007**, *72*, WA3–WA12. [[CrossRef](#)]
32. Constable, S.; Cox, C.S. Marine controlled-source electromagnetic sounding 2. The PEGASUS experiment. *J. Geophys. Res.* **1996**, *101*, 5519–5530. [[CrossRef](#)]
33. Samouëlian, A.; Cousin, I.; Tabbagh, A.; Bruand, A.; Richard, G. Electrical resistivity survey in soil science: A review. *Soil Tillage Res.* **2005**, *83*, 173–193. [[CrossRef](#)]
34. Spangenberg, E. Modeling of the influence of gas hydrate content on the electrical properties of porous sediments. *J. Geophys. Res. Solid Earth* **2001**, *106*, 6535–6548. [[CrossRef](#)]
35. Guo, Z.; Yuan, Y.; Jiang, M.; Liu, J.; Wang, X.; Wang, B. Sensitivity and Resolution of Controlled-Source Electromagnetic Method for Gas Hydrate Stable Zone. *Energies* **2021**, *14*, 8318. [[CrossRef](#)]
36. Lee, K.H.; Jang, H.; Jang, H.; Kim, H.J. Sensitivity analysis of marine controlled-source electromagnetic methods to a shallow gas-hydrate layer with 1D forward modeling. *Geosci. J.* **2011**, *15*, 297–303. [[CrossRef](#)]
37. Noh, K.B.; Kang, S.G.; Seol, S.J.; Byun, J.M. Computation of apparent resistivity from marine controlled-source electromagnetic data for identifying the geometric distribution of gas hydrate. *Geophys. Geophys. Explor.* **2012**, *15*, 75–84. [[CrossRef](#)]
38. Jegen, K.S.A.M. Electromagnetic applications in methane hydrate reservoirs. In *World Atlas of Submarine Gas Hydrates in Continental Margins*; Mienert, J., Berndt, C., Tréhu, A.M., Camerlenghi, A., Liu, C.-S., Eds.; Springer Nature Switzerland AG: Cham, Switzerland, 2022; Volume 44, pp. 73–85.
39. Eidesmo, T.; Ellingsrud, S.; MacGregor, L.M.; Constable, S.; Sinha, M.C.; Johansen, S.; Kong, F.N.; Westerdahl, H. Sea Bed Logging (SBL), a new method for remote and direct identification of hydrocarbon filled layers in deepwater areas. *First Break* **2002**, *20*, 144–152. [[CrossRef](#)]
40. Weitemeyer, K.A.; Constable, S.; Tréhu, A.M. A marine electromagnetic survey to detect gas hydrate at Hydrate Ridge, Oregon. *Geophys. J. Int.* **2011**, *187*, 45–62. [[CrossRef](#)]
41. Riedel, M.; Willoughby, E.; Chen, M.; He, T.; Novosel, I.; Schwalenberg, K.; Hyndman, R.; Spence, G.; Chapman, N.; Edwards, R. Gas hydrate on the northern Cascadia margin: Regional geophysics and structural framework. In *Proceedings of the Integrated Ocean Drilling Program*; IODP: Washington, DC, USA, 2006; p. 28.
42. Gehrman, R.; Schwalenberg, K.; Riedel, M.; Dosso, S.; Mir, R.; Edwards, R. Controlled source electromagnetic study on the response of cold vent sites and gas hydrate occurrences on the northern Cascadia margin. In *AGU Fall Meeting Abstracts*; NASA: Washington, DC, USA, 2012; p. OS43B–1812.
43. Piskunova, E.; Palshin, N.; Yakovlev, D. Electrical conductivity features of the Arctic shelf permafrost and electromagnetic technologies for their studies. *Russ. J. Earth Sci.* **2018**, *18*, 628. [[CrossRef](#)]
44. Attias, E.; Weitemeyer, K.; Minshull, T.A.; Best, A.I.; Sinha, M.; Jegen-Kulcsar, M.; Hölz, S.; Berndt, C. Controlled-source electromagnetic and seismic delineation of subseafloor fluid flow structures in a gas hydrate province, offshore Norway. *Geophys. J. Int.* **2016**, *206*, 1093–1110. [[CrossRef](#)]
45. Myer, D.; Constable, S.; Key, K.; Glinsky, M.E.; Liu, G. Marine CSEM of the Scarborough gas field, Part 1: Experimental design and data uncertainty. *Geophysics* **2012**, *77*, E281–E299. [[CrossRef](#)]

46. Mir, R. Design and Deployment of a Controlled Source EM Instrument on the NEPTUNE Observatory for Long-Term Monitoring of Methane Hydrate Deposits. Ph.D. Thesis, University of Toronto, Toronto, ON, Canada, 2011.
47. Edwards, N.; Mir, R.; Willoughby, E.; Schwalenberg, K.; Scholl, C. The assessment and evolution of offshore gas hydrate deposits using seafloor controlled source electromagnetic methodology. In Proceedings of the OCEANS'10 IEEE SYDNEY, Sydney, NSW, Australia, 5–8 April 2011; pp. 682–686.
48. Anderson, C.; Mattson, J. An integrated approach to marine electromagnetic surveying using a towed streamer and source. *First Break* **2010**, *28*, 38986. [[CrossRef](#)]
49. Yuan, J. Electromagnetic Assessment of Offshore Methane Hydrate Deposits on the Northern Cascadia Margin. Ph.D. Thesis, University of Toronto, Toronto, ON, Canada, 2003.
50. Yuan, J.; Edwards, R.N. The assessment of marine gas hydrates through electrical remote sounding: Hydrate without a BSR? *Geophys. Res. Lett.* **2000**, *27*, 2397–2400. [[CrossRef](#)]
51. Schwalenberg, K.; Willoughby, E.; Mir, R.; Edwards, R. Marine gas hydrate electromagnetic signatures in Cascadia and their correlation with seismic blank zones. *First Break* **2005**, *23*, 26501. [[CrossRef](#)]
52. Constable, S.; Kannberg, P.K.; Weitemeyer, K. Vulcan: A deep-towed CSEM receiver. *Geochem. Geophys. Geosystems* **2016**, *17*, 1042–1064. [[CrossRef](#)]
53. Weitemeyer, K.; Constable, S. Mapping shallow geology and gas hydrate with marine CSEM surveys. *First Break* **2010**, *28*, 97–102. [[CrossRef](#)]
54. Schwalenberg, K.; Gehrman, R.A.; Bialas, J.; Rippe, D. Analysis of marine controlled source electromagnetic data for the assessment of gas hydrates in the Danube deep-sea fan, Black Sea. *Mar. Pet. Geol.* **2020**, *122*, 104650. [[CrossRef](#)]
55. Cheesman, S.J.; Law, L.K.; Louis, B.S. A porosity mapping survey in Hecate Strait using a seafloor electro-magnetic profiling system. *Mar. Geol.* **1993**, *110*, 245–256. [[CrossRef](#)]
56. Ellis, M.; Evans, R.; Hutchinson, D.; Hart, P.; Gardner, J.; Hagen, R. Electromagnetic surveying of seafloor mounds in the northern Gulf of Mexico. *Mar. Pet. Geol.* **2008**, *25*, 960–968. [[CrossRef](#)]
57. Goswami, B.K.; Weitemeyer, K.A.; Minshull, T.A.; Sinha, M.C.; Westbrook, G.K.; Chabert, A.; Henstock, T.J.; Ker, S. A joint electromagnetic and seismic study of an active pockmark within the hydrate stability field at the Vestnesa Ridge, West Svalbard margin. *J. Geophys. Res. Solid Earth* **2015**, *120*, 6797–6822. [[CrossRef](#)]
58. Constable, S.; Lu, R.; Kannberg, P.; Stern, L.A.; Du Frane, W.L.; Roberts, J.J. *In Situ and Laboratory Evidence for High Electrical Anisotropy in Marine Gas Hydrate*; LLNL-TR-8024351006269; Scripps Institute of Oceanography: La Jolla, CA, USA, 2020; p. 7.
59. Kannberg, P.; Constable, S. Characterization and quantification of gas hydrates in the California Borderlands. *Geophys. Res. Lett.* **2020**, *47*, 84703. [[CrossRef](#)]
60. Constable, S.; Weiss, C.J. Mapping thin resistors and hydrocarbons with marine EM methods: Insights from 1D modeling. *Geophysics* **2006**, *71*, G43–G51. [[CrossRef](#)]
61. Ziolkowski, A.; Parr, R.; Wright, D.; Nockles, V.; Limond, C.; Morris, E.; Linfoot, J. Multi-transient electromagnetic repeatability experiment over the North Sea Harding field. *Geophys. Prospect.* **2010**, *58*, 1159–1176. [[CrossRef](#)]
62. Holz, S.; Swidinsky, A.; Sommer, M.; Jegen, M.; Bialas, J. The use of rotational invariants for the interpretation of marine CSEM data with a case study from the North Alex mud volcano, West Nile Delta. *Geophys. J. Int.* **2015**, *201*, 224–245. [[CrossRef](#)]
63. Goto, T.; Kasaya, T.; Takagi, R.; Sakurai, N.; Harada, M.; Sayanagi, K.; Kinoshita, M. Methane hydrate detection with marine electromagnetic surveys: Case studies off Japan coast. In Proceedings of the OCEANS 2009-EUROPE, Bremen, Germany, 11–14 May 2009; pp. 167–170.
64. Commer, M.; Newman, G.A. Three-dimensional controlled-source electromagnetic and magnetotelluric joint inversion. *Geophys. J. Int.* **2009**, *178*, 1305–1316. [[CrossRef](#)]
65. Weitemeyer, K.A.; Constable, S.C.; Key, K.W.; Behrens, J.P. First results from a marine controlled-source electromagnetic survey to detect gas hydrates offshore Oregon. *Geophys. Res. Lett.* **2006**, *33*, 24896. [[CrossRef](#)]
66. Jegen, M.; Hölz, S.; Swidinsky, A.; Sommer, M.; Berndt, C.; Chi, W.-C. Electromagnetic and seismic investigation of methane hydrates offshore Taiwan—The Taiflux experiment. In Proceedings of the OCEANS 2014, Taipei, Taiwan, 7–10 April 2014; pp. 1–4.
67. Ellis, M.; Keirstead, R. Geological parameters effecting controlled-source electromagnetic feasibility: A North Sea sand reservoir example. *SEG Techn. Program Expand. Abstr.* **2011**, *30*, 771–775. [[CrossRef](#)]
68. Gehrman, R.A.; Provenzano, G.; Böttner, C.; Marín-Moreno, H.; Bayrakci, G.; Tan, Y.Y.; Yilo, N.K.; Djanni, A.T.; Weitemeyer, K.A.; Minshull, T.A. Porosity and free gas estimates from controlled source electromagnetic data at the Scanner Pockmark in the North Sea. *Int. J. Greenh. Gas Control* **2021**, *109*, 103343. [[CrossRef](#)]
69. Hsu, S.K.; Chiang, C.W.; Evans, R.L.; Chen, C.S.; Chiu, S.D.; Ma, Y.F.; Chen, S.C.; Tsai, C.H.; Lin, S.S.; Wang, Y. Marine controlled source electromagnetic method used for the gas hydrate investigation in the offshore area of SW Taiwan. *J. Asian Earth Sci.* **2014**, *92*, 224–232. [[CrossRef](#)]
70. Swidinsky, A.; Edwards, R.N.; Jegen, M. The marine controlled source electromagnetic response of a steel borehole casing: Applications for the NEPTUNE Canada gas hydrate observatory. *Geophys. Prospect.* **2013**, *61*, 842–856. [[CrossRef](#)]
71. Jing, J.E.; Wu, Z.L.; Deng, M.; Zhao, Q.X.; Luo, X.H.; Tu, G.H.; Chen, K.; Wang, M. Experiment of marine controlled-source electromagnetic detection in a gas hydrate prospective region of the South China Sea. *Chin. J. Geophys. Acta Geophys. Sin.* **2016**, *59*, 2564–2572. [[CrossRef](#)]

72. Goto, T.-N.; Kasaya, T.; Machiyama, H.; Takagi, R.; Matsumoto, R.; Okuda, Y.; Satoh, M.; Watanabe, T.; Seama, N.; Mikada, H. A marine deep-towed DC resistivity survey in a methane hydrate area, Japan Sea. *Explor. Geophys.* **2008**, *39*, 52–59. [[CrossRef](#)]
73. Evans, R.L. Using CSEM techniques to map the shallow section of seafloor: From the coastline to the edges of the continental slope. *Geophysics* **2007**, *72*, WA105–WA116. [[CrossRef](#)]
74. Key, K.; Constable, S. Coast effect distortion of marine magnetotelluric data: Insights from a pilot study offshore northeastern Japan. *Phys. Earth Planet. Inter.* **2011**, *184*, 194–207. [[CrossRef](#)]
75. Tharimela, R.; Augustin, A.; Ketzer, M.; Cupertino, J.; Miller, D.; Viana, A.; Senger, K. 3D controlled-source electromagnetic imaging of gas hydrates: Insights from the Pelotas Basin offshore Brazil. *Interpretation* **2019**, *7*, SH111–SH131. [[CrossRef](#)]
76. Darnet, M.; Choo, M.C.K.; Plessix, R.E.; Rosenquist, M.L.; Yip-Cheong, K.; Sims, E.; Voon, J.W.K. Detecting hydrocarbon reservoirs from CSEM data in complex settings: Application to deepwater Sabah, Malaysia. *Geophysics* **2007**, *72*, WA97–WA103. [[CrossRef](#)]
77. Jong, J.; Sin, G.H.; McGiveron, S.; Fitton, J. A case study of natural gas hydrates (NGH) in offshore NW Sabah: Identification, shallow geohazard implication for exploration drilling, extraction challenges and potential energy resource estimation. *Bull. Geol. Soc. Malays.* **2020**, *70*, 57–75. [[CrossRef](#)]
78. Hsu, H.-H.; Liu, C.-S.; Chang, Y.-T.; Chang, J.-H.; Ko, C.-C.; Chiu, S.-D.; Chen, S.-C. Diapiric activities and intraslope basin development offshore of SW Taiwan: A case study of the Lower Fangliao Basin gas hydrate prospect. *J. Asian Earth Sci.* **2017**, *149*, 145–159. [[CrossRef](#)]
79. Chuang, P.C.; Yang, T.; Hong, W.L.; Lin, S.; Sun, C.H.; Lin, A.S.; Chen, J.C.; Wang, Y.; Chung, S.H. Estimation of methane flux offshore SW Taiwan and the influence of tectonics on gas hydrate accumulation. *Geofluids* **2010**, *10*, 497–510. [[CrossRef](#)]
80. Swidinsky, A.; Sommer, M.; Hölz, S.; Jegen, M.; Berndt, C.; Chi, W. Electromagnetic imaging of gas hydrate deposits off-shore Taiwan: First results of the Taiflux survey. In Proceedings of the SEG Technical Program Expanded Abstracts 2014, Denver, CO, USA, 26–31 October 2014; pp. 760–764.
81. Davies, M.S.; Dixey, R.; Green, J.C. Evaluation of the effects of extremely low frequency electromagnetic fields on movement in the marine diatom *Amphora coffeaeformis*. *Biol. Bull.* **1998**, *194*, 194–223. [[CrossRef](#)]
82. Tudic, V. Uncertainty evaluation of slope coefficient of high precision displacement sensor. In Proceedings of the Proceedings Elmar-2006, Zadar, Croatia, 7–10 June 2006; pp. 231–234.
83. Yao, R.J.; Yang, J.S. Quantitative evaluation of soil salinity and its spatial distribution using electromagnetic induction method. *Agric. Water Manag.* **2010**, *97*, 1961–1970. [[CrossRef](#)]
84. Kabakchiev, H.; Behar, V.; Garvanov, I.; Kabakchieva, D.; Daniel, L.; Kabakchiev, K.; Gashinova, M.; Cherniakov, M. Experimental verification of maritime target parameter evaluation in forward scatter maritime radar. *Let Radar Sonar Navig.* **2015**, *9*, 355–363. [[CrossRef](#)]
85. Lien, M. Simultaneous joint inversion of amplitude-versus-offset and controlled-source electromagnetic data by implicit representation of common parameter structure. *Geophysics* **2013**, *78*, ID15–ID27. [[CrossRef](#)]
86. Lien, M.; Mannseth, T. Sensitivity study of marine CSEM data for reservoir production monitoring. *Geophysics* **2008**, *73*, F151–F163. [[CrossRef](#)]
87. Schwalenberg, K.; Wood, W.; Pecher, I.; Hamdan, L.; Henrys, S.; Jegen, M.; Coffin, R. Preliminary interpretation of electromagnetic, heat flow, seismic, and geochemical data for gas hydrate distribution across the Porangahau Ridge, New Zealand. *Mar. Geol.* **2010**, *272*, 89–98. [[CrossRef](#)]

Disclaimer/Publisher’s Note: The statements, opinions and data contained in all publications are solely those of the individual author(s) and contributor(s) and not of MDPI and/or the editor(s). MDPI and/or the editor(s) disclaim responsibility for any injury to people or property resulting from any ideas, methods, instructions or products referred to in the content.